

Optimal boundary closures for diagonal-norm upwind SBP operators

Ken Mattsson^{ID}^a, David Niemelä^a, Andrew R. Winters^{ID}^{b,*}

^a*Uppsala University, Department of Information Technology, Uppsala, 75105, Sweden*

^b*Linköping University, Department of Mathematics, Linköping, 58183, Sweden*

Abstract

By employing non-equispaced grid points near boundaries, boundary-optimized upwind finite-difference operators of orders up to nine are developed. The boundary closures are constructed within a diagonal-norm summation-by-parts (SBP) framework, ensuring linear stability on piecewise curvilinear multiblock grids. Boundary and interface conditions are imposed using either weak enforcement through simultaneous approximation terms (SAT) or strong enforcement via the projection method.

The proposed operators yield significantly improved accuracy and computational efficiency compared with SBP operators constructed on equidistant grids. The resulting SBP–SAT and SBP–projection discretizations produce fully explicit systems of ordinary differential equations. The accuracy and stability properties of the proposed operators are demonstrated through numerical experiments for linear hyperbolic problems in one spatial dimension and for the compressible Euler equations in two spatial dimensions.

Keywords: high-order finite difference methods, summation-by-parts operators, artificial dissipation, stability, boundary treatment

1. Introduction

High-order numerical methods are well known to capture transient phenomena more efficiently than first- and second-order methods, as they allow a substantial reduction in the number of degrees of freedom required to achieve a prescribed error tolerance. In particular, high-order finite difference methods are well suited for such problems; see the pioneering work by Kreiss and Oliger [1]. For long-time simulations, it is essential to employ finite difference approximations that do not introduce artificial growth when the underlying partial differential equation is energy bounded, i.e., methods that satisfy *time stability* [2].

For well-posed initial-boundary value problems (IBVPs), a robust and widely used high-order finite difference framework combines summation-by-parts (SBP) operators [3, 4, 5] with either the simultaneous approximation term (SAT) method or the projection method for imposing boundary conditions. The SAT formulation can also be interpreted as a two-point numerical flux formulation; see [6]. The SBP property is independent of the underlying discretization paradigm and has been successfully applied in finite difference, finite volume [7, 8], finite element [3], and discontinuous Galerkin methods [9, 10].

For problems with variable coefficients, such as spatially varying material parameters or discretizations on curvilinear grids, diagonal-norm SBP operators are typically required to guarantee stability unless artificial dissipation (AD) is added to the scheme [11, 12]. Recent developments of the SBP–SAT methodology include [13, 14] and the review papers [15, 16]. Corresponding developments of the SBP–projection methodology are presented in [17, 18].

Most SBP operators available in the literature (see, e.g., [3, 4, 5, 19, 20, 21, 22, 23]) are based on central finite difference stencils with specially designed one-sided boundary closures that mimic the continuous integration-by-parts property in a discrete norm. Traditional diagonal-norm SBP operators, here referring to operators constructed on

*Corresponding author

Email address: andrew.ross.winters@liu.se (Andrew R. Winters ^{ID})

equidistant grids, suffer from reduced formal order of accuracy near boundaries. It has been shown that diagonal-norm SBP operators where all finite difference stencils have accuracy of at least order p are associated with quadrature rules of degree at least $2p - 1$.

To mitigate this boundary accuracy reduction, boundary-optimized SBP operators for first derivatives were introduced in [24] and later improved in [22]. These operators retain p^{th} -order accuracy near boundaries while significantly reducing the leading-order truncation error constant. This improvement is achieved by employing stencils constructed on non-equispaced grid points near the boundaries. More recently, boundary-optimized SBP operators for second derivatives with variable coefficients were presented in [14].

For nonlinear hyperbolic and hyperbolic-parabolic IBVPs, such as the compressible Euler and Navier–Stokes equations, the inclusion of artificial dissipation is often necessary to suppress spurious oscillations. However, the construction of high-order accurate AD operators is nontrivial and typically involves tuning free parameters. The added AD must preserve linear stability, accuracy, and non-stiffness, which requires carefully designed boundary closures. The incorporation of AD within traditional central-difference SBP-SAT discretizations was first analyzed in [25]. The diagonal-norm upwind SBP operators introduced in [26] naturally provide high-order artificial dissipation, effectively damping high-frequency oscillations when combined with standard flux-splitting techniques; see, e.g., [26, 27, 28, 29]. For strongly nonlinear phenomena such as shocks, additional dissipation mechanisms are required. An extension of residual-based artificial viscosity methods to the finite difference SBP-SAT framework is presented in [13].

In addition to their dissipative properties, the upwind SBP operators introduced in [26] provide improved dispersion characteristics for wave propagation problems compared with central-difference SBP operators [30, 31].

The primary contribution of the present work is the derivation of diagonal-norm upwind SBP operators with boundary closures optimized for accuracy. The proposed operators are constructed using non-equispaced boundary grids and are shown to outperform both the standard upwind SBP operators introduced in [26] and the boundary-optimized central-difference SBP operators presented in [22].

In Section 2, the novel upwind SBP definition is presented together with the key steps of its derivation. Section 3 introduces the SBP-projection method for linear hyperbolic problems in one dimension and highlights the differences between traditional and upwind discretizations. In Section 4, the accuracy and stability properties of the optimized upwind SBP operators are verified and compared with previously derived upwind and central-difference SBP operators through numerical simulations of one-dimensional hyperbolic problems. Section 5 presents long-time numerical simulations of an analytical two-dimensional Euler vortex and the Kelvin–Helmholtz instability on multiblock grids to further verify accuracy and stability. Finally, Section 6 summarizes the work. The boundary-optimized upwind SBP operators are provided through the package `SummationByPartsOperators.jl` [32].

2. The finite difference method

The following definitions are required for the present study. We consider real-valued vector functions with k components $\mathbf{u}, \mathbf{v} \in L^2([0, 1])^k$, where

$$\mathbf{u}^T = [u^{(1)}, u^{(2)}, \dots, u^{(k)}], \quad \mathbf{v}^T = [v^{(1)}, v^{(2)}, \dots, v^{(k)}].$$

The continuous weighted inner product on the interval $[x_l, x_r]$ is defined by

$$(\mathbf{u}, \mathbf{v}) = \int_{x_l}^{x_r} \mathbf{u}^T(x) \mathbf{C}(x) \mathbf{v}(x) dx, \quad \mathbf{C}(x) = \mathbf{C}^T(x) > 0,$$

and the corresponding weighted norm is $\|\mathbf{u}\|_C^2 = (\mathbf{u}, \mathbf{u})$.

We discretize the domain $0 \leq x \leq 1$ using m grid points,

$$\mathbf{x} = [x_1, x_2, \dots, x_m]^T,$$

where \mathbf{x} denotes the vector of grid points. For an equidistant grid,

$$x_i = (i - 1)h, \quad i = 1, 2, \dots, m, \quad h = \frac{1}{m - 1}.$$

To improve boundary accuracy, we allow the two grid points closest to each boundary to be non-equidistant. We introduce $d = d_1 + d_2$, where hd_1 is the distance between the first and second grid points and hd_2 is the distance between the second and third grid points. The grid spacing is defined as

$$h = \frac{1}{2d + (m - 5)},$$

where m denotes the total number of grid points. The resulting non-equidistant grid is

$$\mathbf{x} = [0, d_1h, dh, (d + 1)h, (d + 2)h, \dots, (d + (m - 6))h, 1 - dh, 1 - d_1h, 1]^T, \quad (1)$$

where d_1 and d_2 are chosen to minimize boundary truncation errors.

For a system of equations, we define the concatenated discrete solution vector by

$$\mathbf{v}^T = [v^{(1)}, v^{(2)}, \dots, v^{(k)}],$$

where $v^{(j)} = [v_1^{(j)}, v_2^{(j)}, \dots, v_m^{(j)}]$ denotes the discrete solution vector associated with the j^{th} equation. For discrete real-valued vector functions $u, v \in \mathbb{R}^{km}$, we define the discrete inner product

$$(u, v)_{H_k C} = u^T C H_k v,$$

where $H_k = I_k \otimes H$, H is a symmetric positive-definite $m \times m$ matrix, and C denotes the projection of $\mathbf{C}(x)$ onto block-diagonal form. If $\mathbf{C}(x)$ is diagonal, then C is diagonal. Here I_k denotes the $k \times k$ identity matrix. The corresponding norm is $\|v\|_{H_k C}^2 = v^T C H_k v$.

Remark 2.1. The matrix product CH_k defines a norm if and only if it is positive definite. For variable coefficient matrices $\mathbf{C}(x)$, this property can only be guaranteed when the norm matrix H is diagonal; see [11]. Variable coefficients commonly arise from spatially varying material parameters or coordinate transformations associated with curvilinear grids.

We make use of the Kronecker product

$$C \otimes D = \begin{bmatrix} c_{0,0}D & \cdots & c_{0,q-1}D \\ \vdots & & \vdots \\ c_{p-1,0}D & \cdots & c_{p-1,q-1}D \end{bmatrix},$$

where C is a $p \times q$ matrix and D is an $m \times n$ matrix. Two useful identities are

$$(A \otimes B)(C \otimes D) = (AC) \otimes (BD), \quad (A \otimes B)^T = A^T \otimes B^T.$$

The unit basis vectors e_1 and e_m , and the matrix B , are defined by

$$e_1 = [1, 0, \dots, 0]^T, \quad e_m = [0, \dots, 0, 1]^T, \quad B = e_m e_m^T - e_1 e_1^T. \quad (2)$$

In the present study, SBP operators constructed on equidistant grids are referred to as *traditional* SBP operators. Traditional central-difference first-derivative SBP operators were introduced in [3, 4], and traditional second-derivative SBP operators were introduced in [19].

Definition 2.2. *We define a difference operator*

$$D_1 = H^{-1} \left(Q + \frac{B}{2} \right)$$

approximating $\partial/\partial x$ using a p^{th} -order accurate interior stencil as a p^{th} -order first-derivative SBP operator if H is symmetric positive definite and $Q + Q^T = 0$.

2.1. Upwind SBP operators

We define upwind SBP operators [26] as follows.

Definition 2.3. *We define*

$$D_+ = H^{-1} \left(Q_+ + \frac{B}{2} \right), \quad D_- = H^{-1} \left(Q_- + \frac{B}{2} \right),$$

approximating $\partial/\partial x$ using p^{th} -order accurate interior stencils, as p^{th} -order diagonal-norm upwind SBP operators if H is diagonal and positive definite, $Q_+ + Q_-^T = 0$, and $Q_+ + Q_-^T = 2S$ is negative semi-definite.

Traditional upwind SBP operators of both odd and even orders were derived in [26] up to ninth order. The following relations are frequently used:

$$\begin{aligned} \frac{D_+ + D_-}{2} &= H^{-1} \left(\frac{Q_+ + Q_-}{2} + \frac{B}{2} \right) = H^{-1} \left(Q + \frac{B}{2} \right) = D_1, \\ \frac{D_+ - D_-}{2} &= H^{-1} \left(\frac{Q_+ - Q_-}{2} \right) = H^{-1} \left(\frac{Q_+ + Q_-^T}{2} \right) = H^{-1} S, \\ HD_- &= -(D_+)^T H + B, \quad HD_+ = -(D_-)^T H + B, \end{aligned} \quad (3)$$

where $Q = -Q^T$ and $S = S^T \leq 0$. Hence, $(D_+ + D_-)/2$ yields a central SBP approximation of the first derivative, while $(D_+ - D_-)/2$ defines a negative semi-definite operator acting as artificial dissipation.

Next, we derive boundary-optimized upwind SBP operators.

2.2. Boundary-optimized upwind SBP operators

To motivate the construction, we introduce additional notation. Let

$$\hat{D} = H^{-1} \left(\hat{Q} + \frac{B}{2} \right)$$

denote either a traditional first-derivative SBP operator D_1 (Definition 2.2) or an upwind SBP operator D_{\pm} (Definition 2.3). The following two definitions form the foundation of the present work.

Definition 2.4. *Let \mathbf{x}^q denote the grid function obtained by evaluating the polynomial $\frac{x^q}{q!}$ at the grid points. The q^{th} -order error vector is defined by*

$$\mathbf{e}_{(q)} = H \mathbf{x}^{q-1} - \left(\hat{Q} + \frac{B}{2} \right) \mathbf{x}^q. \quad (4)$$

We say that \hat{D} is p^{th} order accurate if $\mathbf{e}_{(q)}$ vanishes for $q = 1, \dots, p$ in the interior and for $q = 1, \dots, s/2$ at the boundaries, where $s = p$ for even p and $s = p - 1$ for odd p .

Definition 2.5. *The discrete ℓ_2 -norm of $\mathbf{e}_{(q)}$ in (4) is defined by*

$$\|\mathbf{e}_{(q)}\|_h^2 = h \mathbf{e}_{(q)}^T \mathbf{e}_{(q)},$$

where h is the grid spacing.

The formal boundary accuracy does not, by itself, fully determine the observed convergence rate. A careful error analysis (not repeated here; see [33]) provides guidance on the expected rates, summarized in the following remark.

Remark 2.6. Svärd and Nordström [33] showed that a stable approximation of an IVP involving derivatives up to order q yields a convergence rate of order $q+b$, where b is the boundary accuracy. Let p denote the interior accuracy of a diagonal-norm SBP operator (traditional or upwind). For first-order hyperbolic problems this implies a convergence rate of order $b+1$. For even p , diagonal-norm boundary closures are restricted to accuracy $b = p/2$ [5], implying that $\mathbf{e}_{(p/2+1)}$ is the leading-order error term. For odd p , the leading-order error term is $\mathbf{e}_{((p-1)/2+1)}$. For example, the eighth- and ninth-order traditional upwind SBP operators have $b = 4$. The numerical experiments in Section 4 indicate that the boundary-optimized operators can yield higher-than-expected convergence rates, in particular for odd orders.

We denote by p the interior order of accuracy. The construction of even-order diagonal-norm upwind (or traditional) SBP operators (up to eighth order) requires at least p boundary points with boundary closures of accuracy $p/2$. Analogously, odd-order upwind (or traditional) SBP operators (up to ninth order) require at least $p-1$ boundary points with boundary closures of accuracy $(p-1)/2$.

2.2.1. Construction procedure

The construction starts by enforcing the required symmetry and SBP compatibility conditions while introducing sufficient degrees of freedom in the boundary closures to meet the accuracy conditions. The operators are derived using Maple (symbolic computations), although any comparable symbolic algebra software can be used.

The interior stencil for the p^{th} -order upwind SBP operator D_+ (and the corresponding $(p+1)^{\text{th}}$ -order operator) is obtained from a central narrow stencil of order $p+2$ by subtracting

$$\frac{h^{p+1}}{\alpha_p} (\Delta_+ \Delta_-)^{p/2+1}$$

to remove the outermost grid point on the left. Here Δ_{\pm} denote the standard forward and backward difference operators, and α_p depends on the order. This yields a $(p+1)$ -order accurate skewed stencil, which is the interior stencil for the $(p+1)^{\text{th}}$ -order upwind SBP operator D_+ . To obtain the interior stencil of the p^{th} -order operator, an additional subtraction is applied to remove the next outermost term on the left, yielding an off-centering by two grid points.

The matrix Q_+ is parameterized by the ansatz

$$\left[\begin{array}{cccccc} q_{1,1} & q_{1,2} & \cdots & q_{1,\tilde{s}} & & \\ q_{2,1} & \ddots & & q_{2,\tilde{s}} & & \\ \vdots & & \vdots & q_{\frac{s}{2}+1} & & \\ \vdots & & \vdots & \vdots & & \\ q_{\tilde{s},1} & q_{\tilde{s},2} & \cdots & q_{\tilde{s},\tilde{s}} & q_1 & \ddots & \ddots \\ & q_{n-\frac{s}{2}} & \cdots & q_0 & q_1 & \cdots & q_{\frac{s}{2}+1} \\ & & \ddots & & \ddots & & \ddots \\ & & & q_{n-\frac{s}{2}} & \cdots & q_0 & q_1 & \cdots & q_{\frac{s}{2}+1} \\ & & & & \ddots & & q_{\tilde{s},\tilde{s}} & q_{\tilde{s}-1,s} & \cdots & q_{1,\tilde{s}} \\ & & & & & \ddots & q_{\tilde{s},\tilde{s}-1} & \ddots & & q_{1,\tilde{s}-1} \\ & & & & & q_{n-\frac{s}{2}} & \vdots & & \vdots & \\ & & & & & & \vdots & & & \vdots \\ & & & & & q_{\tilde{s},1} & \cdots & & & q_{1,1} \end{array} \right].$$

In this work, boundary-optimized upwind SBP operators are derived for $p = 2, 4, 6, 8$ (even orders) and $p = 3, 5, 7, 9$ (odd orders). The first two grid points adjacent to each boundary are non-equidistant. For even orders, $s = p$ and $n = 1$, while for odd orders $s = p - 1$ and $n = 2$ in the above structure. To obtain $s/2$ -accurate boundary closures in both D_+ and D_- , at least s boundary points are required, i.e., $\tilde{s} \geq s$. The operators derived here use the minimal choice $\tilde{s} = s$. The norm matrix is parameterized as

$$H = h \text{diag}(h_1, \dots, h_s, 1, \dots, 1, h_s, \dots, h_1).$$

The grid parameters d_1 and d_2 in (1) are included among the unknowns.

The unknown parameters in \mathbf{x} , Q_+ , and H are determined by enforcing the accuracy requirements in Definition 2.4, together with the SBP symmetry constraints. It is essential that H remains positive definite. For $p > 3$, free parameters remain after enforcing the accuracy and symmetry conditions. The fourth- and fifth-order operators admit four free parameters, the sixth- and seventh-order operators admit six, and the eighth- and ninth-order operators admit eleven.

When selecting these free parameters, two additional objectives are enforced:

- 1) The dissipation matrix $S = \frac{1}{2}(Q_+ + Q_+^T)$ is required to be negative semi-definite.
- 2) Boundary accuracy is optimized by minimizing the leading-order error norm in Definition 2.5.

The resulting nonlinear constraints are solved using a numerical minimization routine in Maple. Multiple local minima may exist, and global optimality cannot be guaranteed. To restrict the search space, the parameters d_1 and d_2 are constrained to lie in $[0.3, 1.7]$, which prevents excessively small boundary spacings that may lead to a large spectral radius. Numerical experiments indicate that it is advantageous to minimize a linear combination of the leading error terms, e.g.,

$$\|\mathbf{e}_{(p/2+1)} + \mathbf{e}_{(p/2+2)}\|_h^2,$$

rather than minimizing only $\|\mathbf{e}_{(p/2+1)}\|_h^2$. After the free parameters have been fixed, the resulting boundary-optimized upwind SBP operators contain no additional tunable parameters.

3. Hyperbolic 1D system

Next, we demonstrate how the upwind SBP operators, in combination with the projection method, are used to construct stable semi-discrete approximations of one-dimensional hyperbolic systems.

3.1. Continuous problem

A stability estimate is derived using an energy method. Consider the hyperbolic system

$$\begin{aligned} \mathbf{C}\mathbf{u}_t + \mathbf{A}\mathbf{u}_x &= 0, & x \in [-1, 1], \quad t \geq 0, \\ u^{(1)}(-1, t) &= 0, & t \geq 0, \\ u^{(1)}(1, t) &= 0, & t \geq 0, \\ \mathbf{u}(x, 0) &= \mathbf{f}(x), & x \in [-1, 1], \end{aligned} \quad (5)$$

where \mathbf{C} is diagonal and positive definite and $\mathbf{f}(x)$ denotes the initial data. The unknown and flux matrix are

$$\mathbf{u} = \begin{bmatrix} u^{(1)} \\ u^{(2)} \end{bmatrix}, \quad \mathbf{A} = \begin{bmatrix} \alpha & 1 \\ 1 & 0 \end{bmatrix}, \quad \alpha \in \mathbb{R}. \quad (6)$$

Multiplying the PDE in (5) by \mathbf{u}^T , integrating by parts, and adding the transpose yields the energy identity

$$\frac{d}{dt} \|\mathbf{u}\|_C^2 = -\mathbf{u}_r^T \mathbf{A} \mathbf{u}_r + \mathbf{u}_l^T \mathbf{A} \mathbf{u}_l = -u_r^{(1)}(\alpha u_r^{(1)} + 2u_r^{(2)}) + u_l^{(1)}(\alpha u_l^{(1)} + 2u_l^{(2)}), \quad (7)$$

where $\mathbf{u}_{l,r}^T = [u_{l,r}^{(1)} \ u_{l,r}^{(2)}]$ denote the boundary traces at $x = -1$ and $x = 1$, respectively. Imposing $u^{(1)}(\pm 1, t) = 0$ gives

$$\frac{d}{dt} \|\mathbf{u}\|_C^2 = 0,$$

and the problem is therefore energy stable. In the following, we assume $\alpha \geq 0$.

3.2. Semi-discrete problem

An SBP discretization of (5) using the upwind SBP operators D_{\pm} is given by

$$\begin{aligned} Cv_t + D_x v &= 0, & t \geq 0, \\ (e^{(1)} \otimes e_1^T) v &= 0, & t \geq 0, \\ (e^{(1)} \otimes e_m^T) v &= 0, & t \geq 0, \\ v &= f, & t = 0, \end{aligned} \quad (8)$$

where $e^{(1)} = [1 \ 0]$. The boundary operator is defined as

$$L = \begin{bmatrix} e^{(1)} \otimes e_1^T \\ e^{(1)} \otimes e_m^T \end{bmatrix},$$

and the discrete spatial operator is given by

$$D_x = \begin{bmatrix} \alpha D_- & D_+ \\ D_- & 0 \end{bmatrix}.$$

The SBP-projection approximation of (8) is

$$\begin{aligned} v_t + PC^{-1}D_xPv &= 0, & t \geq 0, \\ v &= f, & t = 0, \end{aligned} \quad (9)$$

where the projection operator is given by

$$P = I - \bar{H}^{-1}L^T(L\bar{H}^{-1}L^T)^{-1}L, \quad \bar{H} = H_2C.$$

The SBP structure follows from

$$H_2D_x = \begin{bmatrix} \alpha Q_- + \alpha \frac{B}{2} & Q_+ + \frac{B}{2} \\ Q_- + \frac{B}{2} & 0 \end{bmatrix},$$

where B is defined in (2). Hence,

$$H_2D_x + (H_2D_x)^T = \bar{B} = \begin{bmatrix} -2\alpha S + \alpha B & B \\ B & 0 \end{bmatrix}. \quad (10)$$

Remark 3.1. For central-difference SBP operators, replacing D_{\pm} by D_1 in D_x yields

$$H_2D_x + (H_2D_x)^T = \bar{B} = \begin{bmatrix} \alpha B & B \\ B & 0 \end{bmatrix}.$$

The identity $\bar{H}P = P^T\bar{H}$ is used in the subsequent discrete energy analysis. Introducing the projected variables $w = Pv$, multiplying (9) by $v^T\bar{H}$, and adding the transpose gives

$$\begin{aligned} \frac{d}{dt} \|v\|_{\bar{H}}^2 &= -(Pv)^T (H_2D_x + (H_2D_x)^T)(Pv) \\ &= -w^T \bar{B} w \\ &= -w_m^{(1)} (\alpha w_m^{(1)} + 2w_m^{(2)}) + w_1^{(1)} (\alpha w_1^{(1)} + 2w_1^{(2)}) + 2\alpha (w^{(1)})^T S w^{(1)}. \end{aligned} \quad (11)$$

Since $Lw = 0$, the projected solution satisfies the boundary conditions exactly, i.e., $w_1^{(1)} = w_m^{(1)} = 0$, and therefore

$$\frac{d}{dt} \|v\|_{\bar{H}}^2 = 2\alpha (w^{(1)})^T S w^{(1)} \leq 0,$$

where the inequality follows from the defining property $S = S^T \leq 0$ of the upwind SBP operators. For central-difference SBP operators, $S = 0$, i.e., no dissipation is introduced for $\alpha > 0$.

4. Computations in 1D

We investigate convergence using a smooth analytical solution for $\alpha = 0$ and compare the proposed boundary-optimized upwind SBP operators with the traditional upwind SBP operators presented in [26]. For completeness, we also compare with traditional central-difference SBP operators D_1 and the corresponding boundary-optimized D_1 operators derived in [22], for orders up to twelve.

Robustness is further examined by introducing convection through $\alpha = 3$, which leads to the development of non-smooth solution features after boundary interaction. In all numerical experiments, we set C equal to the identity matrix.

4.1. Spectral radius

We first compare the spectral radius of the SBP-projection approximation (9) for $\alpha = 0$. The discretization matrix is given by

$$M = -PC^{-1}D_xP.$$

Table 1 reports the spectral radius of the normalized matrix hM , comparing the traditional upwind SBP operators from [26] with the proposed boundary-optimized upwind SBP operators. The eighth-order boundary-optimized upwind operator exhibits a comparatively large spectral radius and is therefore expected to be less efficient for explicit time integration.

Table 1: The spectral radius of $h M$ comparing traditional upwind and the boundary-optimized upwind SBP operators.

| Operator | $p = 4$ | $p = 6$ | $p = 8$ |
|-----------------------------------|---------|---------|---------|
| Traditional upwind, order p | 2.6652 | 3.1060 | 2.3706 |
| Traditional upwind, order $p + 1$ | 1.6234 | 1.7452 | 2.0260 |
| Optimized upwind, order p | 2.6310 | 2.5732 | 17.6784 |
| Optimized upwind, order $p + 1$ | 1.9280 | 2.4187 | 2.7045 |

4.2. Convergence

The accuracy of the SBP-projection approximation (9) is verified against an analytical solution in which a narrow Gaussian pulse propagates and reflects at the boundaries. In this section we set $\alpha = 0$, corresponding to pure wave propagation without convection.

Let $u(t_*)$ and $u_{(m)}$ denote the analytical and numerical solutions at time $t = t_*$, evaluated on a grid with m points. The error vector is defined as

$$\mathbf{err}_{(m)} = \mathbf{u}(t_*) - \mathbf{u}_{(m)},$$

and the discrete ℓ^2 -norm of the error is

$$\|\mathbf{err}_{(m)}\|_h = \sqrt{h} \|\mathbf{err}_{(m)}\|.$$

The observed convergence rate, denoted by q , is computed as

$$q = \log_{10} \left(\frac{\|\mathbf{err}_{(m)}\|_h}{\|\mathbf{err}_{(n)}\|_h} \right) / \log_{10} \left(\frac{n}{m} \right), \quad (12)$$

where m and n denote two successive grid resolutions.

The Gaussian profiles

$$\theta^{(1)}(x, t) = \exp \left(- \left(\frac{x - t}{r_*} \right)^2 \right), \quad \theta^{(2)}(x, t) = - \exp \left(- \left(\frac{x + t}{r_*} \right)^2 \right),$$

are introduced, where r_* defines the pulse width. The initial data are set to

$$u^{(1)}(x, 0) = \theta^{(1)}(x, 0) - \theta^{(2)}(x, 0), \quad u^{(2)}(x, 0) = \theta^{(1)}(x, 0) + \theta^{(2)}(x, 0). \quad (13)$$

On a domain of length $L = 2$, the analytical solution to (5) with $\alpha = 0$ and initial data (13) is given by

$$u^{(1)}(x, t) = \theta^{(2)}(x, L - t) - \theta^{(1)}(x, L - t), \quad u^{(2)}(x, t) = \theta^{(1)}(x, L - t) + \theta^{(2)}(x, L - t),$$

after the Gaussian pulses have been reflected at the boundaries, i.e., for $t \in [L - L/8, L + L/8]$.

We set $r_* = 0.1$ and integrate to $t = t_* = 1.8$ using the classical four-stage, fourth-order Runge–Kutta method [34] with CFL number 0.05, i.e., $k = 0.05 h$, so that temporal errors are negligible compared with spatial errors. Table 2 reports convergence for traditional central-difference SBP operators of orders 6–12, and Table 3 reports the corresponding results for boundary-optimized central-difference SBP operators. Tables 4 and 6 report convergence for the boundary-optimized upwind SBP operators, while Tables 5 and 7 report results for the traditional upwind SBP operators.

Table 2: $\log(\ell^2$ errors) and convergence rates for (9) using even-order (6th–12th) traditional central-difference SBP operators from [5], CFL=0.05.

| m | $\log l^2_{(6)}$ | q | $\log l^2_{(8)}$ | q | $\log l^2_{(10)}$ | q | $\log l^2_{(12)}$ | q |
|-----|------------------|------|------------------|------|-------------------|------|-------------------|------|
| 51 | -1.05 | — | -0.83 | — | -0.72 | — | -0.58 | — |
| 101 | -1.74 | 2.28 | -2.09 | 4.18 | -1.98 | 4.19 | -1.53 | 3.16 |
| 201 | -2.87 | 3.77 | -3.47 | 4.60 | -3.43 | 4.82 | -3.22 | 5.62 |
| 401 | -4.27 | 4.66 | -4.83 | 4.49 | -5.24 | 6.01 | -5.46 | 7.43 |

Table 3: $\log(\ell^2$ errors) and convergence rates for (9) using even-order (6th–12th) boundary-optimized central-difference SBP operators from [22], CFL=0.05.

| m | $\log l^2_{(6)}$ | q | $\log l^2_{(8)}$ | q | $\log l^2_{(10)}$ | q | $\log l^2_{(12)}$ | q |
|-----|------------------|------|------------------|------|-------------------|------|-------------------|-------|
| 51 | -1.18 | — | -1.55 | — | -1.85 | — | -1.97 | — |
| 101 | -2.70 | 5.05 | -3.59 | 6.77 | -4.27 | 8.04 | -4.42 | 8.16 |
| 201 | -4.47 | 5.88 | -5.94 | 7.80 | -7.20 | 9.72 | -7.55 | 10.40 |
| 401 | -6.25 | 5.90 | -8.28 | 7.77 | -9.51 | 7.68 | -10.73 | 10.57 |

Table 4: $\log(\ell^2$ errors) and convergence rates for (9) using even-order (4th–8th) boundary-optimized upwind SBP operators derived herein, CFL=0.05.

| m | $\log l^2_{(4)}$ | q | $\log l^2_{(6)}$ | q | $\log l^2_{(8)}$ | q |
|-----|------------------|------|------------------|------|------------------|------|
| 51 | -0.39 | — | -1.19 | — | -2.10 | — |
| 101 | -1.17 | 2.60 | -2.78 | 5.30 | -4.27 | 7.20 |
| 201 | -2.32 | 3.82 | -4.56 | 5.93 | -6.65 | 7.88 |
| 401 | -3.52 | 3.98 | -6.37 | 5.99 | -9.05 | 7.98 |

Table 5: $\log(\ell^2$ errors) and convergence rates for (9) using even-order (4th–8th) traditional upwind SBP operators from [26], CFL=0.05.

| m | $\log l^2_{(4)}$ | q | $\log l^2_{(6)}$ | q | $\log l^2_{(8)}$ | q |
|-----|------------------|------|------------------|------|------------------|------|
| 51 | -0.42 | — | -0.65 | — | -1.28 | — |
| 101 | -1.20 | 2.60 | -2.70 | 6.78 | -3.64 | 7.86 |
| 201 | -2.34 | 3.78 | -5.21 | 8.36 | -6.41 | 9.20 |
| 401 | -3.53 | 3.96 | -6.80 | 5.27 | -9.40 | 9.92 |

Table 6: $\log(\ell^2$ errors) and convergence rates for (9) using odd-order (5th–9th) boundary-optimized upwind SBP operators derived herein, CFL=0.05.

| m | $\log l^2_{(5)}$ | q | $\log l^2_{(7)}$ | q | $\log l^2_{(9)}$ | q |
|-----|------------------|------|------------------|------|------------------|-------|
| 51 | -1.22 | — | -2.01 | — | -2.48 | — |
| 101 | -2.88 | 5.50 | -4.31 | 7.67 | -5.70 | 10.72 |
| 201 | -4.69 | 6.00 | -6.71 | 7.96 | -8.82 | 10.36 |
| 401 | -6.50 | 6.03 | -9.11 | 7.97 | -11.76 | 9.77 |

Table 7: $\log(\ell^2$ errors) and convergence rates for (9) using odd-order (5th–9th) traditional upwind SBP operators from [26], CFL=0.05.

| m | $\log l^2_{(5)}$ | q | $\log l^2_{(7)}$ | q | $\log l^2_{(9)}$ | q |
|-----|------------------|------|------------------|------|------------------|------|
| 51 | -0.78 | — | -1.12 | — | -1.36 | — |
| 101 | -2.27 | 4.94 | -2.79 | 5.54 | -3.53 | 7.20 |
| 201 | -3.89 | 5.37 | -5.15 | 7.84 | -6.20 | 8.88 |
| 401 | -5.43 | 5.14 | -7.28 | 7.09 | -8.90 | 8.98 |

The expected convergence rates are 3, 4, 5, 6, and 7 for even-order SBP operators of orders 4, 6, 8, 10, and 12, respectively. For odd-order SBP operators of orders 5, 7, and 9, the expected convergence rates are 3, 4, and 5. At coarse

and moderate resolutions, the boundary-optimized operators—in particular the proposed upwind SBP operators—exhibit substantially higher observed convergence rates. The boundary-optimized odd-order upwind SBP operators demonstrate especially strong accuracy at marginal resolution.

4.3. Non-smooth boundary interaction

We next set $\alpha = 3$, which yields predominantly right-going waves. After interaction with the right boundary, the solution develops non-smooth features. The initial data are again given by (13).

We set $r_* = 0.1$ and integrate to $t = t_* = 1.8$ using the classical four-stage, fourth-order Runge–Kutta method with CFL number 0.05. Two grid resolutions are considered, $m = 201$ and $m = 401$. We compare the traditional 12th-order central SBP operator with the boundary-optimized 12th-order central SBP operator and the boundary-optimized 9th-order upwind SBP operator. The results are shown in Figure 1.

5. Computations in 2D

Next, the newly derived upwind SBP operators are applied to nonlinear two-dimensional problems. To this end, the compressible Euler equations are considered,

$$\partial_t \begin{pmatrix} \rho \\ \rho v_1 \\ \rho v_2 \\ \rho e \end{pmatrix} + \partial_x \begin{pmatrix} \rho v_1 \\ \rho v_1^2 + p \\ \rho v_1 v_2 \\ (\rho e + p)v_1 \end{pmatrix} + \partial_y \begin{pmatrix} \rho v_2 \\ \rho v_1 v_2 \\ \rho v_2^2 + p \\ (\rho e + p)v_2 \end{pmatrix} = 0, \quad (14)$$

describing the motion of an ideal gas with density ρ , velocity components v_1 and v_2 , and total energy density ρe . The pressure is given by

$$p = (\gamma - 1) \left(\rho e - \frac{1}{2} \rho (v_1^2 + v_2^2) \right), \quad (15)$$

where the ratio of specific heats is set to $\gamma = 1.4$. For all numerical experiments presented below, periodic boundary conditions are imposed on multi-block Cartesian meshes.

The spatial discretizations are implemented in Trixi.jl [35, 36], where the boundary-optimized upwind SBP operators are provided through the package SummationByPartsOperators.jl [32]. Time integration is performed using explicit Runge–Kutta methods from OrdinaryDiffEq.jl [37]; the specific schemes employed are described in the respective subsections. Visualization of the numerical solutions is carried out using ParaView [38].

5.1. Isentropic vortex

To examine the convergence properties of the boundary-optimized upwind SBP operators for a two-dimensional nonlinear problem, we consider the classical isentropic vortex test case introduced by Shu [39]. The analytical solution for given values of x , y , and t is

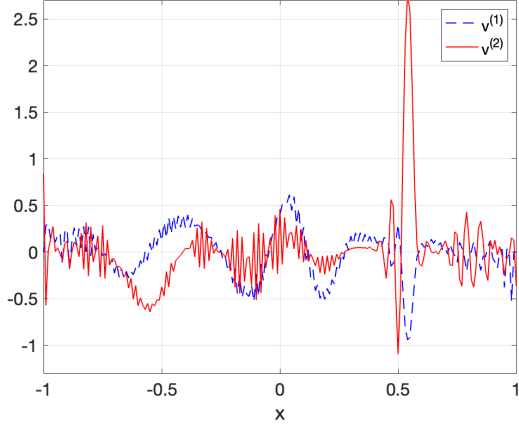
$$\begin{aligned} \rho &= \left(1 - \frac{\varepsilon^2(\gamma - 1)M^2}{8\pi^2} \exp(f(x, y, t)) \right)^{1/(\gamma-1)}, & p &= \frac{\rho^\gamma}{\gamma M^2}, \\ v_1 &= 1 - \frac{\varepsilon(y - y_0)}{2\pi} \exp\left(\frac{f(x, y, t)}{2}\right), & v_2 &= \frac{\varepsilon(x - x_0 - t)}{2\pi} \exp\left(\frac{f(x, y, t)}{2}\right), \end{aligned} \quad (16)$$

where

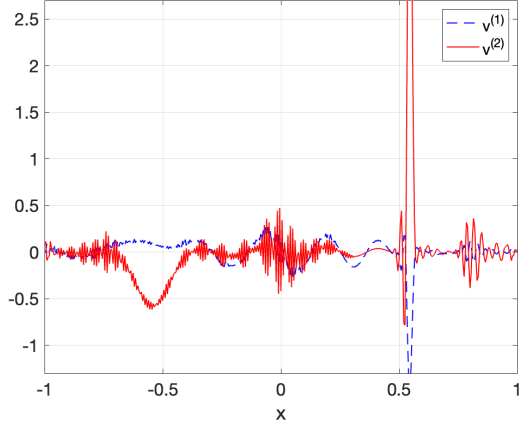
$$f(x, y, t) = 1 - \left((x - x_0 - t)^2 + (y - y_0)^2 \right).$$

Here, M denotes the Mach number, (x_0, y_0) specifies the initial vortex position, and ε is the nondimensional circulation controlling the vortex strength. The initial condition is obtained by evaluating the vortex solution at $t = 0$.

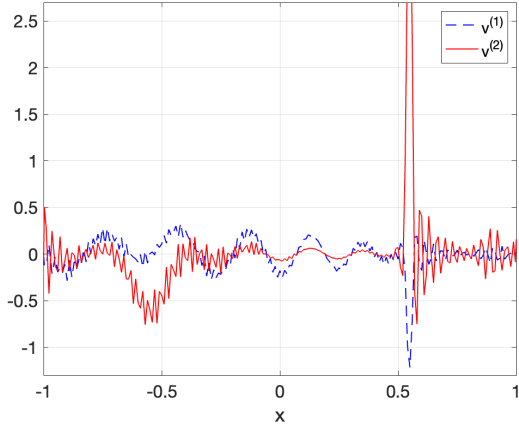
The isentropic vortex is simulated on a two-dimensional chevron-shaped domain depicted in Figure 2. The domain is decomposed into two blocks; an example configuration using 21×21 grid points in each block is shown in Figure 2. The node distribution associated with the boundary-optimized discretization is non-uniform. A mapping between



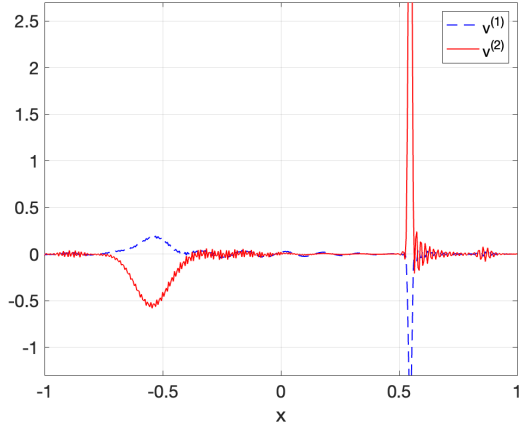
(a) $m = 201$, traditional SBP central 12th order



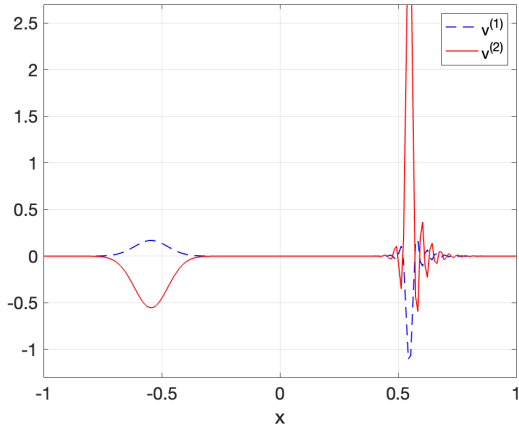
(b) $m = 401$, traditional SBP central 12th order



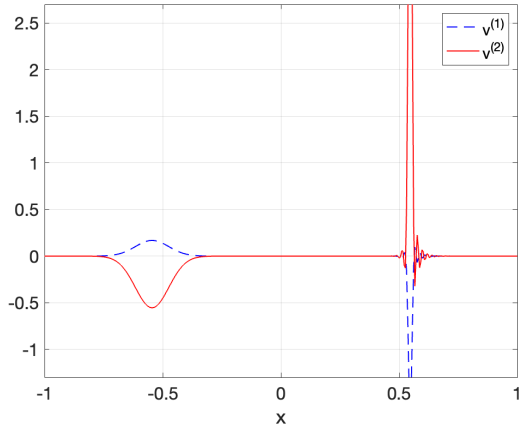
(c) $m = 201$, optimal SBP central 12th order



(d) $m = 401$, optimal SBP central 12th order



(e) $m = 201$, optimal SBP upwind 9th order



(f) $m = 401$, optimal SBP upwind 9th order

Figure 1: Comparing central difference SBP (both traditional and boundary-optimized) against the boundary-optimized 9th-order upwind SBP operator for two grid resolutions. The simulations are run to $t = 1.8$ with $CFL=0.05$ and $\alpha = 3$.

computational and physical coordinates is applied in each block, introducing metric terms into the discretization; see, e.g., [24].

The initial vortex position is set to $(x_0, y_0) = (0, -0.5)$ such that the block interface, where discontinuities in the metric terms occur, intersects the vortex [24]. The vortex propagates from left to right across the slanted periodic boundaries. The isentropic vortex provides an analytical solution to the compressible Euler equations provided that the final simulation time is sufficiently small to prevent interaction with the periodic boundaries. Accordingly, for the convergence study, the final time is chosen as $t = 1$, ensuring that boundary effects do not influence the solution. For the convergence experiments, the Mach number is set to $M = 0.5$ and the vortex strength to $\varepsilon = 5$.

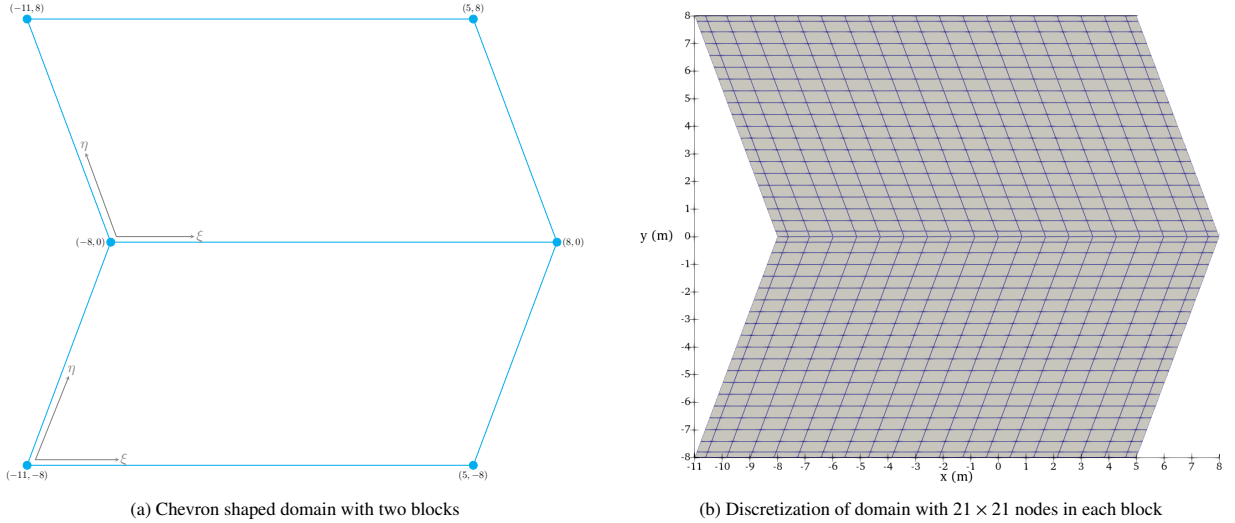


Figure 2: Domain for the isentropic vortex convergence test and an example discretization of the two block domain with a non-uniform grid.

For the upwind discretizations, the local Lax–Friedrichs flux vector splitting for the compressible Euler equations is employed [6]. Coupling for standard SBP discretizations is performed using the local Lax–Friedrichs numerical flux function, which is equivalent to an upwind simultaneous approximation term (SAT).

Time integration of the semidiscrete system is carried out using the fourth-order accurate, nine-stage Runge–Kutta method proposed by Ranocha et al. [40], combined with error-based step-size control and a sufficiently small tolerance of 10^{-12} . This tolerance ensures that temporal errors are negligible and that the numerical approximation is dominated by spatial discretization errors.

Convergence results with respect to the density ρ are presented for the boundary-optimized upwind SBP operators of odd and even orders in Tables 8 and 9, respectively. For comparison, the same convergence analysis is performed using the traditional upwind SBP operators from [26], with results reported in Tables 10 and 11.

Table 8: $\log(l^2)$ errors) and convergence rates for the isentropic vortex using odd order (3rd–9th) boundary optimized upwind SBP operators

| m | $\log l^2_{(3)}$ | q | $\log l^2_{(5)}$ | q | $\log l^2_{(7)}$ | q | $\log l^2_{(9)}$ | q |
|-----|------------------|------|------------------|------|------------------|------|------------------|------|
| 34 | -2.89 | — | -3.26 | — | -3.36 | — | -3.45 | — |
| 68 | -3.73 | 2.78 | -4.57 | 4.33 | -4.87 | 5.03 | -5.00 | 5.17 |
| 136 | -4.63 | 3.01 | -5.83 | 4.19 | -6.31 | 4.77 | -6.53 | 5.06 |
| 272 | -5.53 | 2.99 | -7.14 | 4.36 | -7.99 | 5.57 | -8.51 | 6.60 |
| 544 | -6.41 | 2.98 | -8.49 | 4.47 | -9.81 | 6.08 | -10.72 | 7.32 |

Table 9: $\log(l^2)$ errors and convergence rates for the isentropic vortex using even order (2nd–8th) boundary optimized upwind SBP operators

| m | $\log l^2_{(2)}$ | q | $\log l^2_{(4)}$ | q | $\log l^2_{(6)}$ | q | $\log l^2_{(8)}$ | q |
|-----|------------------|------|------------------|------|------------------|------|------------------|------|
| 34 | -2.36 | — | -3.13 | — | -3.40 | — | -3.51 | — |
| 68 | -2.85 | 1.61 | -4.00 | 2.92 | -4.49 | 3.62 | -4.71 | 3.99 |
| 136 | -3.41 | 1.86 | -5.07 | 3.55 | -5.95 | 4.83 | -6.30 | 5.26 |
| 272 | -4.00 | 1.98 | -6.27 | 3.99 | -7.61 | 5.53 | -8.19 | 6.29 |
| 544 | -4.61 | 2.00 | -7.49 | 4.04 | -9.41 | 5.99 | -10.38 | 7.28 |

Table 10: $\log(l^2)$ errors and convergence rates for the isentropic vortex using odd order (3rd–9th) upwind SBP operators [26]

| m | $\log l^2_{(3)}$ | q | $\log l^2_{(5)}$ | q | $\log l^2_{(7)}$ | q | $\log l^2_{(9)}$ | q |
|-----|------------------|------|------------------|------|------------------|------|------------------|------|
| 34 | -2.88 | — | -3.22 | — | -3.26 | — | -3.13 | — |
| 68 | -3.69 | 2.69 | -4.40 | 3.92 | -4.53 | 4.25 | -4.44 | 4.36 |
| 136 | -4.54 | 2.82 | -5.52 | 3.71 | -5.76 | 4.09 | -6.15 | 5.67 |
| 272 | -5.36 | 2.73 | -6.58 | 3.50 | -7.02 | 4.17 | -7.94 | 5.95 |
| 544 | -6.16 | 2.65 | -7.59 | 3.39 | -8.28 | 4.18 | -9.68 | 5.8 |

Table 11: $\log(l^2)$ errors and convergence rates for the isentropic vortex using even order (2nd–8th) upwind SBP operators [26]

| m | $\log l^2_{(2)}$ | q | $\log l^2_{(4)}$ | q | $\log l^2_{(6)}$ | q | $\log l^2_{(8)}$ | q |
|-----|------------------|------|------------------|------|------------------|------|------------------|------|
| 34 | -2.36 | — | -3.09 | — | -3.22 | — | -3.13 | — |
| 68 | -2.85 | 1.62 | -3.99 | 2.99 | -4.40 | 3.93 | -4.42 | 4.31 |
| 136 | -3.41 | 1.86 | -5.06 | 3.55 | -5.73 | 4.42 | -6.13 | 5.65 |
| 272 | -4.00 | 1.98 | -6.24 | 3.91 | -7.04 | 4.37 | -7.93 | 6.00 |
| 544 | -4.61 | 2.00 | -7.40 | 3.86 | -8.32 | 4.23 | -9.73 | 5.95 |

The convergence studies presented in Tables 8–11 demonstrate that the boundary-optimized upwind SBP operators achieve significantly improved convergence rates, particularly at marginal resolution. This behavior is especially pronounced for the odd-order upwind SBP operators derived herein. The two-dimensional nonlinear convergence tests confirm the enhanced convergence behavior observed for the one-dimensional linear results in Section 4.2.

Next, the robustness and accuracy properties of the boundary-optimized upwind SBP operators are examined. Time integration is performed using error-based step-size control with absolute and relative tolerances set to 10^{-7} . Smaller tolerances were also tested, but no qualitative differences in robustness were observed. For this comparison, an 8th-order diagonal-norm SBP operator is employed on a 61×61 grid in each block, such that the isentropic vortex is only marginally resolved.

In addition to the boundary-optimized upwind SBP operators developed in this work, the following operators are considered for comparison: traditional SBP operators [5], boundary-optimized traditional SBP operators [22], and the upwind SBP operators from [26]. For the initial comparison, the same vortex parameters are used, and the solution is advanced to a final time of $t = 75$, corresponding to approximately seven vortex passages through the periodic domain.

Figure 3 illustrates the vortex solution obtained using each operator. The traditional SBP operator becomes unstable early in the simulation at $t \approx 0.2919$, whereas the boundary-optimized traditional SBP operator remains stable until approximately $t \approx 41.438$. This indicates that improved boundary accuracy enhances the robustness of the discretization. Both the traditional and boundary-optimized upwind SBP operators remain stable until the final time. However, small discrepancies are observed in the solution obtained with the traditional upwind operator that are not present when using the boundary-optimized upwind SBP operator.

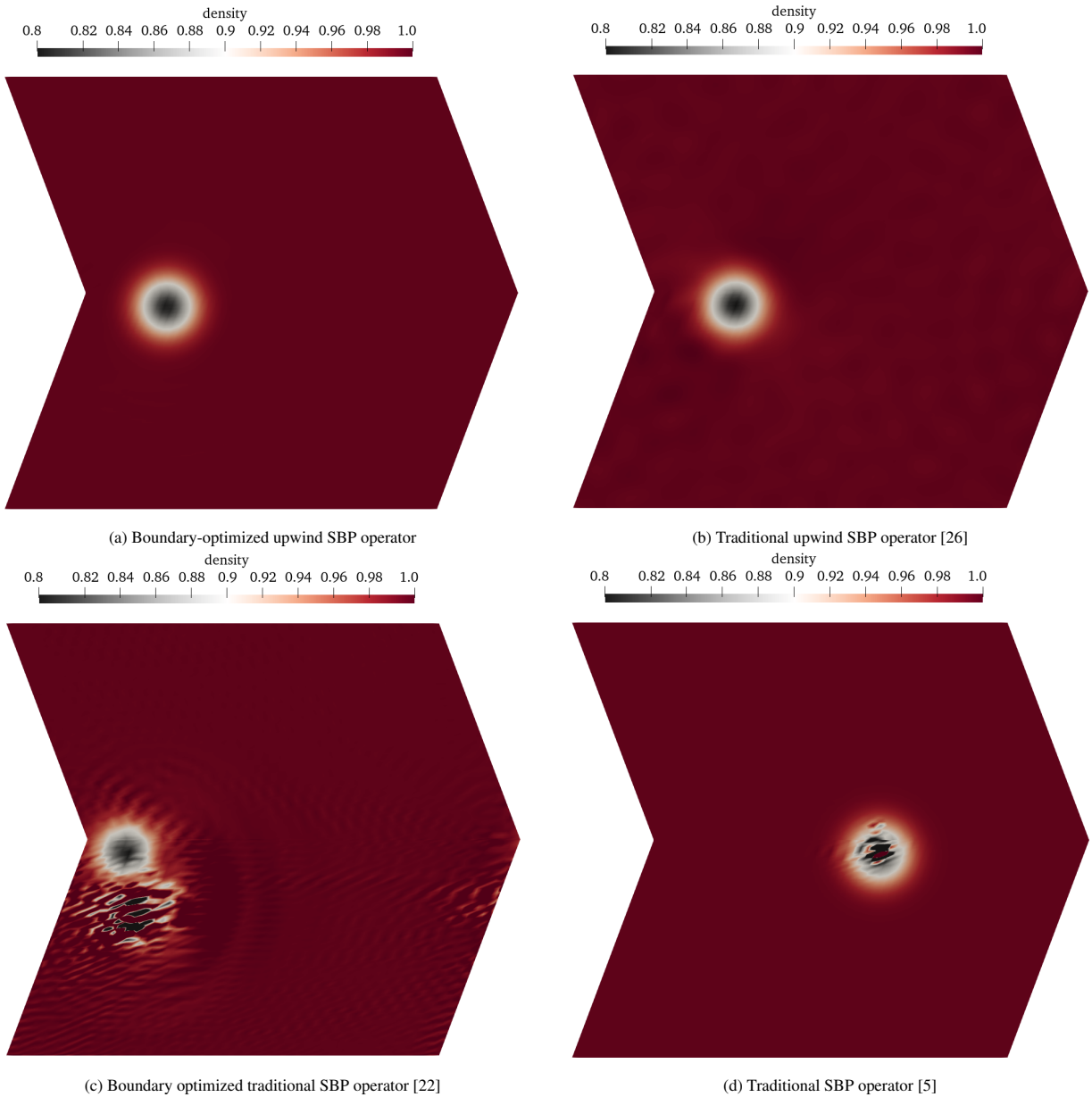
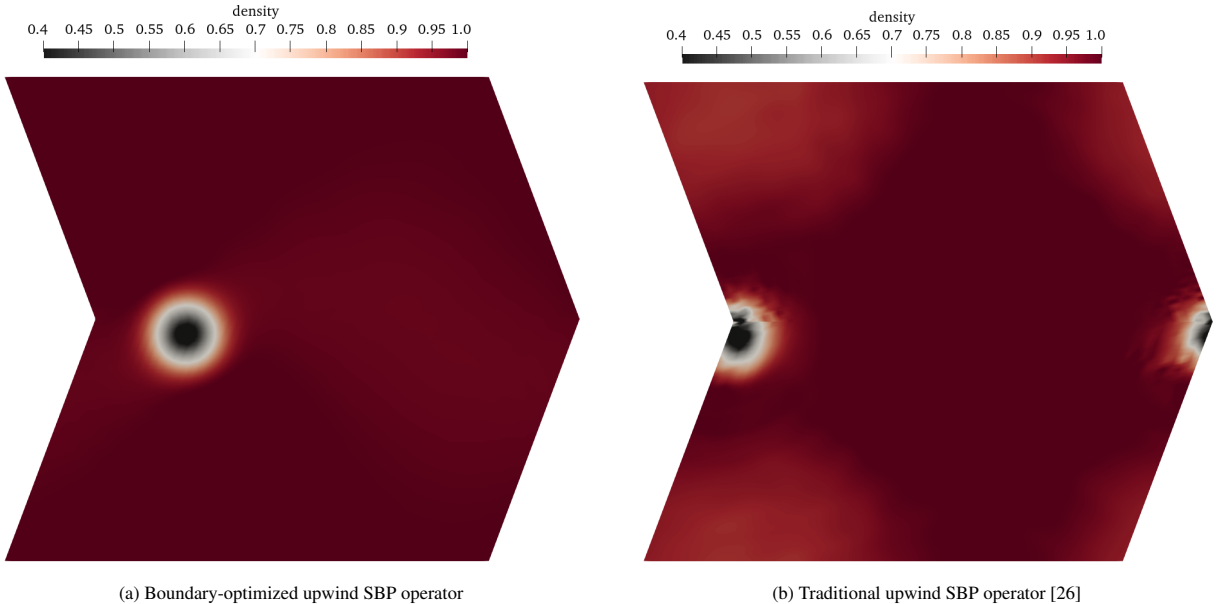


Figure 3: Isentropic vortex on a chevron domain with two blocks each containing 61×61 nodes. The vortex strength is $\varepsilon = 5$. All results use 8th order diagonal norm SBP operators with 4th order boundary stencils. The boundary optimized upwind (a) and traditional upwind SBP operators run to the final time $t = 75$, although the traditional upwind operator exhibits small discrepancies. The boundary optimized traditional SBP operator crashes at $t \approx 41.438$ and the traditional SBP operator crashes early in the simulation at $t \approx 0.2919$.

To further investigate this behavior, the vortex strength is increased by setting $\varepsilon = 10$. The simulations are again performed using both the traditional and boundary-optimized upwind SBP operators and advanced to the final time $t = 75$. The boundary-optimized operators remain stable throughout the simulation, whereas the traditional upwind SBP operator becomes unstable at approximately $t \approx 72.255$, as shown in Figure 4.

As in the previous experiment, the instability originates near the block interface where the vortex intersects the boundary. This observation further indicates that improved boundary accuracy enhances the robustness of the discretization.



(a) Boundary-optimized upwind SBP operator

(b) Traditional upwind SBP operator [26]

Figure 4: Isentropic vortex on a chevron domain with two blocks each containing 61×61 nodes. The vortex strength is $\varepsilon = 10$. The 8th order boundary optimized upwind SBP operator (left) runs to the final time $t = 75$ whereas the traditional 8th order upwind SBP operator (right) crashes at $t \approx 72.255$.

5.2. Kelvin-Helmholtz instability

As a final test, we consider a Kelvin–Helmholtz instability (KHI) setup for the two-dimensional compressible Euler equations of an ideal fluid to further examine the robustness of the boundary-optimized upwind SBP operators for under-resolved flows. Specifically, we employ the initial condition proposed by Chan et al. [41],

$$\rho = \frac{1}{2} + \frac{3}{4}B(x, y), \quad v_1 = \frac{1}{2}(B(x, y) - 1), \quad v_2 = \frac{1}{10}\sin(2\pi x), \quad p = 1, \quad (17)$$

where $B(x, y)$ is the smoothed approximation

$$B(x, y) = \tanh(15y + 7.5) - \tanh(15y - 7.5) \quad (18)$$

to a discontinuous step function. The computational domain is $[-1, 1]^2$ with time interval $t \in [0, 15]$.

Among the available flux vector splittings for the compressible Euler equations, the Steger–Warming splitting [42] is employed for the KHI tests. Alternative splittings, including the local Lax–Friedrichs and van Leer–Hänel splittings [43, 44, 45], were also tested and produced qualitatively similar results.

Time integration of the semidiscrete system is performed using the third-order, four-stage strong-stability-preserving (SSP) Runge–Kutta method [46, 47] combined with the error-based step-size controller proposed in [40]. Error-based time stepping is applied with absolute and relative tolerances set to 10^{-6} .

A resolution study similar to those presented in [6, 48] is conducted. The number of nodes per element is fixed while the number of elements is increased to refine the resolution. Specifically, the number of nodes is set to $m = 17$ in each spatial direction, corresponding to the minimum number of points required to construct boundary-optimized upwind SBP operators with interior orders $p = 8$ and $p = 9$.

Table 12 summarizes the final simulation times obtained using the boundary-optimized upwind SBP operators and the traditional upwind SBP operators from [26].

First, it is observed that all upwind SBP methods with a small number of elements, $K \in \{1, 4\}$, successfully complete the simulation. Furthermore, the boundary-optimized upwind SBP operators derived herein reach the final simulation time for lower interior orders of accuracy, $p \in \{2, 3, 4\}$. Overall, the boundary-optimized upwind SBP operators demonstrate improved robustness compared with their traditional counterparts. However, consistent with

Table 12: Final times of numerical simulations of the Kelvin-Helmholtz instability with K elements using 17 nodes per coordinate direction for the upwind SBP methods. Final times less than 15 indicate that the simulation crashed.

| (a) Boundary-optimized upwind SBP operator | | | | | | | | | | (b) Traditional upwind SBP operator [26] | | | | | | | | | |
|--|----------------------------|----|----|------|------|------|------|------|------|--|----------------------------|----|------|------|------|------|------|------|--|
| K | interior order of accuracy | | | | | | | | | K | interior order of accuracy | | | | | | | | |
| | 2 | 3 | 4 | 5 | 6 | 7 | 8 | 9 | | | 2 | 3 | 4 | 5 | 6 | 7 | 8 | 9 | |
| 1 | 15 | 15 | 15 | 15 | 15 | 15 | 15 | 15 | | 1 | 15 | 15 | 15 | 15 | 15 | 15 | 15 | 15 | |
| 4 | 15 | 15 | 15 | 15 | 15 | 15 | 15 | 15 | | 4 | 15 | 15 | 15 | 15 | 15 | 15 | 15 | 15 | |
| 16 | 15 | 15 | 15 | 15 | 15 | 15 | 15 | 4.06 | 4.95 | 16 | 15 | 15 | 15 | 15 | 15 | 1.99 | 1.79 | 1.71 | |
| 64 | 15 | 15 | 15 | 3.83 | 3.89 | 3.84 | 4.27 | 4.23 | | 64 | 15 | 15 | 4.52 | 3.83 | 3.73 | 3.71 | 2.38 | 1.92 | |
| 256 | 15 | 15 | 15 | 3.70 | 15 | 3.60 | 3.63 | 3.56 | | 256 | 15 | 15 | 5.76 | 3.67 | 3.63 | 3.62 | 3.50 | 3.50 | |

the observations reported in [6], simulations employing larger numbers of elements and higher orders of accuracy become unstable and terminate before $t = 5$ for all upwind SBP operators.

The improved robustness of the boundary-optimized upwind SBP operators can be attributed to increased accuracy near element boundaries. Instabilities in traditional upwind SBP operators typically originate near element interfaces, where unphysical solution states (e.g., negative densities) may arise and ultimately lead to simulation failure. The improved boundary accuracy of the boundary-optimized operators enhances the propagation of wave-like solution structures across element interfaces.

This behavior is illustrated in Figure 5, which shows the Kelvin-Helmholtz solution at final time $t = 3.63$. The simulation uses a 16×16 Cartesian mesh (so $K = 256$) with 17 nodes in each spatial direction per element and 6th order accurate upwind SBP operators. From the last row in Table 12, this configuration remains stable for the boundary-optimized upwind SBP operators but becomes unstable for the traditional upwind SBP operators. The regions highlighted in bright green in Figure 5(b) correspond to locations where the density becomes negative in the simulation using the traditional upwind SBP operators. These regions are concentrated near element boundaries.

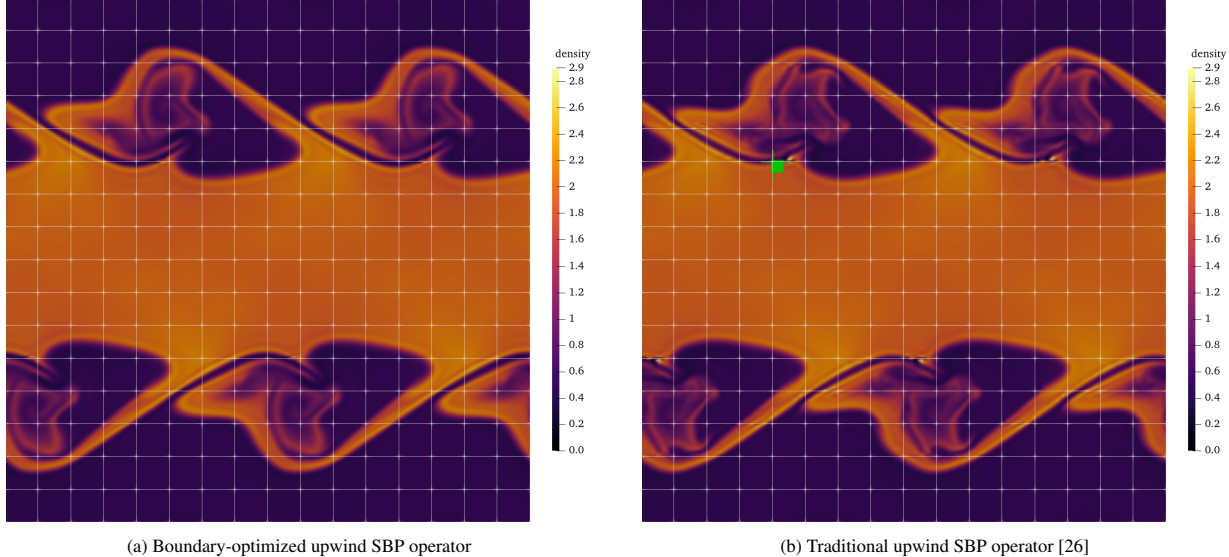


Figure 5: Visualization of numerical solutions from Kelvin-Helmholtz instability simulations at time $t = 3.63$. We use interior order $p = 6$ upwind SBP operators on a mesh of 16^2 Cartesian elements with 17^2 nodes per element. The boundary-optimized simulation reaches the final time, whereas the traditional one crashes; green regions in (b) mark points with negative density.

6. Conclusions

The primary objective of this work has been the construction of boundary-optimized diagonal-norm upwind SBP operators that provide built-in artificial dissipation when combined with flux vector splitting techniques for hyperbolic

systems. Boundary and interface conditions are imposed using either the projection method or the simultaneous approximation term (SAT) technique.

The proposed boundary-optimized upwind SBP operators yield robust and accurate discretizations for hyperbolic problems, as demonstrated through numerical experiments involving both linear and nonlinear systems. For wave propagation problems, the numerical results show that the boundary-optimized diagonal-norm upwind SBP operators outperform both boundary-optimized central SBP operators and traditional upwind SBP operators. The observed convergence rates for linear first-order wave equations exceed the theoretical expectations.

Improved convergence behavior and accuracy, particularly for marginally resolved discretizations, are also observed for nonlinear two-dimensional simulations of the compressible Euler equations. Furthermore, the boundary-optimized upwind SBP operators demonstrate enhanced robustness for complex but smooth Kelvin–Helmholtz instability simulations compared with traditional upwind SBP operators based on uniform-grid stencils.

Future work will investigate the efficiency and robustness of the proposed upwind SBP operators in more complex settings, including curvilinear geometries and three-dimensional domains.

CRediT authorship contribution statement

Ken Mattsson: Conceptualization; Formal analysis; Investigation; Methodology; Data curation; Visualization; Software; Writing - original draft **David Niemelä:** Conceptualization; Methodology; Software; Writing - review & editing **Andrew R. Winters:** Conceptualization; Funding acquisition; Supervision; Visualization; Software; Writing - review & editing

Data Availability

Data is available upon request to the corresponding author.

Declaration of competing interest

The authors declare that they have no known competing financial interests or personal relationships that could have appeared to influence the work reported in this paper.

Acknowledgement

Ken Mattsson was partially supported by the Swedish Research Council (grant 2021-05830 VR), and FORMAS (grant 2022-00843).

David Niemelä was supported by the Swedish Research Council (grant 2021-05830 VR) and FORMAS (grant 2022-00843).

Andrew Winters was supported by the Swedish Research Council (grant 2020-03642 VR).

References

- [1] H.-O. Kreiss, J. Oliger, Comparison of accurate methods for the integration of hyperbolic equations, *Tellus* XXIV (1972) 199–215.
- [2] B. Gustafsson, *High Order Difference Methods for Time Dependent PDE*, Springer, 2007. doi:10.1007/978-3-540-74993-6.
URL <https://books.google.com/books?id=guaT5yPiLAGc>
- [3] H.-O. Kreiss, G. Scherer, Finite element and finite difference methods for hyperbolic partial differential equations, in: C. d. Boor (Ed.), *Mathematical Aspects of Finite Elements in Partial Differential Equations*, Academic Press, 1974, pp. 195 – 212. doi:<https://doi.org/10.1016/B978-0-12-208350-1.50012-1>
URL <https://www.sciencedirect.com/science/article/pii/B9780122083501500121>
- [4] B. Strand, Summation by parts for finite difference approximations for d/dx , *J. Comput. Physics* 110 (1994) 47–67.
- [5] K. Mattsson, J. Nordström, Summation by parts operators for finite difference approximations of second derivatives, *J. Comput. Phys.* 199(2) (2004) 503–540.
- [6] H. Ranocha, A. R. Winters, M. Schlottke-Lakemper, P. Öffner, J. Glaubitz, G. J. Gassner, On the robustness of high-order upwind summation-by-parts methods for nonlinear conservation laws, *Journal of Computational Physics* 520 (2025) 113471.
- [7] F. Ham, K. Mattsson, G. Iaccarino, Accurate and stable finite volume operators for unstructured flow solvers, *Annual Research Briefs* 243 (2006).

[8] J. Nordström, K. Forsberg, C. Adamsson, P. Eliasson, Finite volume methods, unstructured meshes and strict stability for hyperbolic problems, *Applied Numerical Mathematics* 45 (4) (2003) 453–473.

[9] A. R. Winters, D. A. Kopriva, G. J. Gassner, F. Hindenlang, Construction of modern robust nodal discontinuous Galerkin spectral element methods for the compressible Navier–Stokes equations, in: M. Kronbichler, P.-O. Persson (Eds.), *Efficient High-Order Discretizations for Computational Fluid Dynamics*, Springer International Publishing, 2021, pp. 117–196.

[10] G. J. Gassner, A skew-symmetric discontinuous Galerkin spectral element discretization and its relation to SBP-SAT finite difference methods, *SIAM Journal on Scientific Computing* 35 (3) (2013) A1233–A1253.

[11] M. Svärd, On coordinate transformation for summation-by-parts operators, *Journal of Scientific Computing* 20(1) (2004).

[12] K. Mattsson, M. Almquist, A solution to the stability issues with block norm summation by parts operators, *J. Comput. Phys.* 253 (2013) 418–442.

[13] V. Stiernström, L. Lundgren, M. Nazarov, K. Mattsson, A residual-based artificial viscosity finite difference method for scalar conservation laws, *Journal of Computational Physics* 430 (2021) 110100. doi:<https://doi.org/10.1016/j.jcp.2020.110100>. URL <https://www.sciencedirect.com/science/article/pii/S0021999120308743>

[14] V. Stiernström, M. Almquist, K. Mattsson, Boundary-optimized summation-by-parts operators for finite difference approximations of second derivatives with variable coefficients, *Journal of Computational Physics* 491 (2023) 112376. doi:<https://doi.org/10.1016/j.jcp.2023.112376>. URL <https://www.sciencedirect.com/science/article/pii/S0021999123004710>

[15] D. C. D. R. Fernández, J. E. Hicken, D. W. Zingg, Review of summation-by-parts operators with simultaneous approximation terms for the numerical solution of partial differential equations, *Computers & Fluids* 95 (2014) 171 – 196. doi:<http://dx.doi.org/10.1016/j.compfluid.2014.02.016>. URL <http://www.sciencedirect.com/science/article/pii/S0045793014000796>

[16] M. Svärd, J. Nordström, Review of summation-by-parts-operators schemes for initial-boundary-value problems, *Journal of Computational Physics* 268 (0) (2014) 17 – 38. doi:<http://dx.doi.org/10.1016/j.jcp.2014.02.031>. URL <http://www.sciencedirect.com/science/article/pii/S002199911400151X>

[17] K. Mattsson, P. Olsson, An improved projection method, *Journal of Computational Physics* 372 (2018) 349 – 372. doi:<https://doi.org/10.1016/j.jcp.2018.06.030>. URL <http://www.sciencedirect.com/science/article/pii/S002199911830408X>

[18] G. Eriksson, K. Mattsson, Weak versus strong wall boundary conditions for the incompressible navier-stokes equations, *Journal of Scientific Computing* 92 (3) (2022) 81. doi:<10.1007/s10915-022-01941-5>. URL <https://doi.org/10.1007/s10915-022-01941-5>

[19] K. Mattsson, Summation by parts operators for finite difference approximations of second-derivatives with variable coefficients, *Journal of Scientific Computing* 51 (2012) 650–682. doi:<10.1007/s10915-011-9525-z>. URL <http://dx.doi.org/10.1007/s10915-011-9525-z>

[20] K. Mattsson, Diagonal-norm summation by parts operators for finite difference approximations of third and fourth derivatives, *J. Comput. Phys.* 274 (0) (2014) 432 – 454. doi:<http://dx.doi.org/10.1016/j.jcp.2014.06.027>. URL <http://www.sciencedirect.com/science/article/pii/S0021999114004343>

[21] V. Linders, M. Kupiainen, J. Nordstrom, Summation-by-parts operators with minimal dispersion error for coarse grid flow calculations, *Journal of Computational Physics* 340 (2017) 160–176. doi:<10.1016/j.jcp.2017.03.039>

[22] K. Mattsson, M. Almquist, E. van der Weide, Boundary optimized diagonal-norm SBP operators, *Journal of Computational Physics* (2018). doi:<https://doi.org/10.1016/j.jcp.2018.06.010>. URL <http://www.sciencedirect.com/science/article/pii/S0021999118303887>

[23] D. C. Del Rey Fernández, P. D. Boom, D. W. Zingg, A generalized framework for nodal first derivative summation-by-parts operators, *J. Comput. Phys.* 266 (2014) 214–239. doi:<10.1016/j.jcp.2014.01.038>. URL <http://dx.doi.org/10.1016/j.jcp.2014.01.038>

[24] K. Mattsson, M. Almquist, M. H. Carpenter, Optimal diagonal-norm SBP operators, *J. Comput. Phys.* 264 (2014) 91–111.

[25] K. Mattsson, M. Svärd, J. Nordström, Stable and Accurate Artificial Dissipation, *Journal of Scientific Computing* 21(1) (2004) 57–79.

[26] K. Mattsson, Diagonal-norm upwind SBP operators, *Journal of Computational Physics* 335 (2017) 283 – 310. doi:<http://dx.doi.org/10.1016/j.jcp.2017.01.042>. URL <http://www.sciencedirect.com/science/article/pii/S002199911730058X>

[27] L. Lundgren, K. Mattsson, An efficient finite difference method for the shallow water equations, *Journal of Computational Physics* 422 (2020) 109784. doi:<https://doi.org/10.1016/j.jcp.2020.109784>. URL <https://www.sciencedirect.com/science/article/pii/S0021999120305581>

[28] K. Duru, D. Stewart, N. Lee, A dual-pairing summation-by-parts finite difference framework for nonlinear conservation laws, arXiv preprint arXiv:2411.06629 (2024).

[29] J. K. J. Hew, K. Duru, S. Roberts, C. Zoppou, K. Ricardo, Strongly stable dual-pairing summation by parts finite difference schemes for the vector invariant nonlinear shallow water equations—I: Numerical scheme and validation on the plane, *Journal of Computational Physics* 523 (2025) 113624.

[30] K. Mattsson, O. O'Reilly, Compatible diagonal-norm staggered and upwind sbp operators, *Journal of Computational Physics* 352 (Supplement C) (2018) 52 – 75. doi:<https://doi.org/10.1016/j.jcp.2017.09.044>. URL <http://www.sciencedirect.com/science/article/pii/S0021999117307040>

[31] C. Williams, K. Duru, Full-spectrum dispersion relation preserving summation-by-parts operators, *SIAM Journal on Numerical Analysis* 62 (4) (2024) 1565–1588.

[32] H. Ranocha, SummationByPartsOperators.jl: A Julia library of provably stable semidiscretization techniques with mimetic properties, *Journal of Open Source Software* 6 (64) (2021) 3454. doi:<10.21105/joss.03454>. URL <https://github.com/ranocha/SummationByPartsOperators.jl>

[33] M. Svärd, J. Nordström, On the convergence rates of energy-stable finite-difference schemes, *Journal of Computational Physics* 397 (2019) 108819. doi:<https://doi.org/10.1016/j.jcp.2019.07.018>.
URL <https://www.sciencedirect.com/science/article/pii/S0021999119305030>

[34] J. Butcher, *Numerical Methods for Ordinary Differential Equations*, 2nd Edition, John Wiley & Sons, 2008.

[35] H. Ranocha, M. Schlottke-Lakemper, A. R. Winters, E. Faulhaber, J. Chan, G. Gassner, Adaptive numerical simulations with Trixi.jl: A case study of Julia for scientific computing, *Proceedings of the JuliaCon Conferences* 1 (1) (2022) 77. [arXiv:2108.06476](https://arxiv.org/abs/2108.06476), doi:10.21105/jcon.00077.

[36] M. Schlottke-Lakemper, A. R. Winters, H. Ranocha, G. J. Gassner, A purely hyperbolic discontinuous Galerkin approach for self-gravitating gas dynamics, *Journal of Computational Physics* 442 (2021) 110467. [arXiv:2008.10593](https://arxiv.org/abs/2008.10593), doi:10.1016/j.jcp.2021.110467.

[37] C. Rackauckas, Q. Nie, DifferentialEquations.jl – A performant and feature-rich ecosystem for solving differential equations in Julia, *Journal of Open Research Software* 5 (1) (2017) 15. doi:10.5334/jors.151.

[38] J. Ahrens, B. Geveci, C. Law, ParaView: An end-user tool for large-data visualization, in: *The Visualization Handbook*, Elsevier, 2005, pp. 717–731.

[39] C.-W. Shu, Essentially non-oscillatory and weighted essentially non-oscillatory schemes for hyperbolic conservation laws, Final Report NASA/CR-97-206253, NASA, Institute for Computer Applications in Science and Engineering, NASA Langley Research Center, Hampton VA United States (11 1997).

[40] H. Ranocha, L. Dalcin, M. Parsani, D. I. Ketcheson, Optimized Runge-Kutta methods with automatic step size control for compressible computational fluid dynamics, *Communications on Applied Mathematics and Computation* 4 (2021) 1191–1228. [arXiv:2104.06836](https://arxiv.org/abs/2104.06836), doi:10.1007/s42967-021-00159-w.

[41] J. Chan, H. Ranocha, A. M. Rueda-Ramirez, G. J. Gassner, T. Warburton, On the entropy projection and the robustness of high order entropy stable discontinuous Galerkin schemes for under-resolved flows, *Frontiers in Physics* 10 (07 2022). [arXiv:2203.10238](https://arxiv.org/abs/2203.10238), doi:10.3389/fphy.2022.898028.

[42] J. L. Steger, R. Warming, Flux vector splitting of the inviscid gasdynamic equations with application to finite difference methods, Technical Memorandum NASA/TM-78605, NASA, NASA Ames Research Center; Moffett Field, CA, United States (1979).

[43] B. van Leer, Flux-vector splitting for the Euler equations, in: E. Krause (Ed.), *Eighth International Conference on Numerical Methods in Fluid Dynamics*, Vol. 170 of *Lecture Notes in Physics*, Springer, Berlin, Heidelberg, 1982, pp. 507–512. doi:10.1007/3-540-11948-5_66.

[44] D. Hänel, R. Schwane, G. Seider, On the accuracy of upwind schemes for the solution of the Navier-Stokes equations, in: *8th Computational Fluid Dynamics Conference*, American Institute of Aeronautics and Astronautics, 1987, p. 1105. doi:10.2514/6.1987-1105.

[45] M.-S. Liou, C. J. Steffen Jr, High-order polynomial expansions (HOPE) for flux-vector splitting, Technical Memorandum NASA/TM-104452, NASA, NASA Lewis Research Center; Cleveland, OH, United States (1991).

[46] J. F. B. M. Kraaijevanger, Contractivity of Runge-Kutta methods, *BIT Numerical Mathematics* 31 (3) (1991) 482–528. doi:10.1007/BF01933264.

[47] S. Conde, I. Fekete, J. N. Shadid, Embedded pairs for optimal explicit strong stability preserving Runge-Kutta methods, *Journal of Computational and Applied Mathematics* 412 (2022) 114325. [arXiv:1806.08693](https://arxiv.org/abs/1806.08693), doi:10.1016/j.cam.2022.114325.

[48] J. Glaubitz, H. Ranocha, A. R. Winters, M. Schlottke-Lakemper, P. Öffner, G. Gassner, Generalized upwind summation-by-parts operators and their application to nodal discontinuous Galerkin methods, *Journal of Computational Physics* 529 (2025) 113841.